



# High selectivity in visible-light-driven partial photocatalytic oxidation of benzyl alcohol into benzaldehyde over single-crystalline rutile TiO<sub>2</sub> nanorods

Cong-Ju Li<sup>a,b,\*</sup>, Guo-Rong Xu<sup>a,b</sup>, Baohong Zhang<sup>a</sup>, Jian Ru Gong<sup>a,\*\*</sup>

<sup>a</sup> National Center for Nanoscience and Technology, 11 Zhongguancun Beiyitiao, Beijing 100190, China

<sup>b</sup> College of Material Science and Engineering, Beijing Institute of Fashion Technology, Beijing 100029, China

## ARTICLE INFO

### Article history:

Received 16 September 2011

Received in revised form

21 November 2011

Accepted 3 December 2011

Available online 9 December 2011

### Keywords:

Selective photocatalysis

Single-crystalline

Rutile TiO<sub>2</sub>

Benzyl alcohol

## ABSTRACT

Selective photocatalysis offers an alternative green approach for valuable fine chemical synthesis and environmental remediation. In this work, high selectivity in visible-light-driven partial photocatalytic oxidation of benzyl alcohol over single-crystalline rutile TiO<sub>2</sub> nanorods was achieved. The nanorods were prepared by a hydrothermal reaction using rutile TiO<sub>2</sub> nanofibers obtained from calcination of composite electrospun nanofibers as a substrate. The selectivity of partial photocatalytic oxidation of benzyl alcohol over the obtained rutile TiO<sub>2</sub> nanorods under visible-light irradiation was over 99%, much better than the results reported over nanoparticle counterparts under UV light irradiation. A tentative reaction mechanism was proposed, that is, benzyl alcohol was first adsorbed on the surface of rutile TiO<sub>2</sub> to form a complex which could absorb visible-light to generate electrons and holes, then was oxidized into the benzaldehyde by electrons transfer and holes-attracted release of H atom. In addition, the unidirectional property of nanorods favored the electron transfer and thus the selectivity. To the best of our knowledge, it is the first report of the rutile TiO<sub>2</sub> nanorods for the visible-light-driven selective photocatalysis. Our work extends the selective photocatalysts to one-dimensional nanomaterials instead of limiting to the commonly used nanoparticles and will open up an intriguing perspective for green synthesis and efficient energy conversion.

© 2011 Elsevier B.V. All rights reserved.

## 1. Introduction

Environmental protection and energy saving are crucial issues to the whole world at present. As an advanced and environmental friendly process, photocatalysis over semiconductor photocatalysts has proven to be very effective in the field of environmental remediation and energy conversion [1–8]. Compared with traditional chemical methods, photocatalysis can be carried out in absence of toxic and corrosive reagents. However, the strong oxidative potential of radicals and holes generated on the surface of photocatalysts always promote a complete mineralization, which makes photocatalysis unselective.

Recently, semiconductor photocatalysts were reported to be applied in the partial oxidation/reduction process, for example, oxidation of –CH<sub>2</sub>OH to –CHO instead of CO<sub>2</sub> and H<sub>2</sub>O [9–12]. The above reaction is named as selective photocatalytic conversion or partial photocatalysis in terminology [11,12], which has become an vital embranchment in photocatalytic area due to its potential

applications for the green synthesis of fine chemicals and efficient energy conversion [13–16].

Oxidation of aromatic alcohols to aldehydes is of great significance in selective photocatalytic conversion because of the importance of aromatic aldehydes as raw materials for many useful chemicals, such as dye, resin, fragrance and drugs. Semiconductor photocatalysts, mainly TiO<sub>2</sub> nanoparticles, were confirmed to be effective in oxidation of benzyl alcohol to benzaldehyde, and it was concluded that the properties of TiO<sub>2</sub> and the adsorption mode of organic molecule on the TiO<sub>2</sub> surface were the two main factors affecting the selective photocatalytic activity [17–20]. Recently, Palmisano group [9,12,15,19,21–23] performed comprehensive and systematical work in the photocatalytic oxidation of aromatic alcohols to aldehydes in water with home prepared both rutile and anatase TiO<sub>2</sub> nanoparticles under UV light irradiation. The results showed 45–74% of selectivity over rutile TiO<sub>2</sub> nanoparticles for photo-oxidation of 4-substituted aromatic alcohols to the corresponding aldehydes [19], 41% and 62% of selectivity over anatase and rutile TiO<sub>2</sub> nanoparticles for oxidation of 4-methoxy benzyl alcohols, respectively [10,21], and 60% over rutile TiO<sub>2</sub> nanoparticles for oxidation of benzyl alcohols to benzaldehyde [12]. Mul et al. [24–26] also investigated the effect of surface and physical properties of TiO<sub>2</sub> nanoparticles on the selective photocatalytic activity under UV light irradiation.

\* Corresponding author at: National Center for Nanoscience and Technology, 11 Zhongguancun Beiyitiao, Beijing 100190, China.

\*\* Corresponding author.

E-mail addresses: [congju1@gmail.com](mailto:congju1@gmail.com) (C.-J. Li), [gongjr@nanoctr.cn](mailto:gongjr@nanoctr.cn) (J.R. Gong).

In order to make efficient use of light energy, light used for irradiation in selective photocatalytic oxidation over semiconductor photocatalysts needs to be transferred from UV light to visible-light since UV light constitutes only 4% of solar light. Therefore, some researchers have worked on visible-light-driven selective photocatalytic oxidation of aromatic alcohols to aldehydes. For example, Zhang et al. introduced a system of dye-sensitized anatase TiO<sub>2</sub>-TEMPO (2,2,6,6-tetramethylpiperidinyloxy) nanoparticles which showed selectivity of over 93% for oxidation of a series of aromatic alcohols and of as high as 98% for benzyl alcohols under visible-light irradiation [27]. Higashimoto et al. systematically studied selective photocatalytic oxidation of aromatic alcohols to aldehydes under visible-light irradiation over anatase TiO<sub>2</sub> nanoparticles, which showed a selectivity of >99% for most of the detected aromatic alcohols [20,28,29].

Rutile TiO<sub>2</sub> also attracted much attention for selective photocatalysis [19,22] thanks to the most stable property among the three crystalline conformations of TiO<sub>2</sub>, while the activities studied were mainly focused on nanoparticles [15]. It is worth noting that one-dimensional (1D) TiO<sub>2</sub> nanomaterials are especially appealing for applications in a wide range of areas, including photocatalysis, solar cells, and sensors, due to the high surface-to-volume ratio [30], superior electrons survivability [31], and well-defined unidirectional channel for electrical carrier transport [32], which is helpful for light harvesting. Therefore, in the current work, single-crystalline rutile TiO<sub>2</sub> nanorods were successfully fabricated by hydrothermal method, which has proved to be very applicable in materials synthesis [33,34]. And then the selective photocatalytic activity of the obtained rutile TiO<sub>2</sub> nanorods in oxidation of benzyl alcohol into benzaldehyde under visible-light irradiation was investigated in this work. In addition, a tentative mechanism for partial photocatalysis over TiO<sub>2</sub> nanorods was proposed. To the best of our knowledge, it is the first report of the selective photocatalytic oxidation of aromatic alcohols over the 1D nanomaterials under visible-light irradiation.

## 2. Experimental

### 2.1. Sample preparation

In the preparation of the substrate, 4 g of polyvinyl-pyrrolidone (PVP, Sinopharm Chemical Reagent Co., Ltd.) was dissolved in 15 ml of anhydrous ethanol (Beijing Chemical Works) under magnetic stirring to form homogeneous solution, then added a mixed solution of 1 ml of Ti(OBu)<sub>4</sub> and 1 ml of acetic acid (Beijing Chemical Works) to form electrospinning solution. Electrospinning process was carried out on a typical electrospinning apparatus at room temperature. A syringe pump (Harvard Apparatus, PHD ULTRA™, Instech Solomon, USA) with a syringe containing electrospinning solution was used as the impetus supplier at the rate of 3 ml h<sup>-1</sup>. The positive high voltage applied on the needle of the syringe was 9–11 kV and the distance between the syringe needle and collecting plate was 13–15 cm. The obtained composite electrospinning nanofibers were then calcined at the temperature of 900 °C for 2 h to obtain the rutile TiO<sub>2</sub> substrate.

In the hydrothermal reaction process, 1 ml of Ti(OBu)<sub>4</sub> was firstly dropped into the mixed solution of 15 ml of deionized water and 15 ml of chloric acid (36–38 wt%, Beijing Chemical Works), then 10 mg of rutile TiO<sub>2</sub> substrate was added into the solution. After stirring under ultrasonic condition for 5 min, the solution was transferred into an autoclave, held at a temperature of 150 °C for 4, 8, 12, 16, 20, and 24 h, and the corresponding rutile TiO<sub>2</sub> nanorods samples obtained were marked as S1, S2, S3, S4, S5, and S6, respectively. The schematic illustration of the process of the sample preparation is shown in Fig. S1 in Supporting Information.

### 2.2. Characterization

X-ray diffraction patterns (XRD) of samples were recorded using D/MAX-2500 diffractometer (Rigaku, Japan) with Cu K $\alpha$  radiation ( $\lambda = 1.54056 \text{ \AA}$ ) to determine the phase composition and the crystallinity, and the accelerating voltage and beam current were 50 kV and 300 mA, respectively. Scanning electron microscopy (SEM) images were collected on a field emission SEM (FESEM, S-4800, Hitachi, Japan). Transmission electron microscopy (TEM) images were collected on an F20 S-TWIN electron microscope (Technai G2, FEI Co.) with an accelerating voltage of 200 kV. In order to observe the surface chemical groups of samples, the Fourier transform infrared spectroscopy (FTIR) analysis of samples was carried out on FTIR analyzer (Spectrum one, USA). UV-vis absorption spectra of S1 and S1 adsorbed with benzyl alcohol were measured on a TU-1901 UV-vis spectrophotometer over the wavelength range of 300–600 nm. S1 adsorbed with benzyl alcohol was obtained as follows: S1 was first suspended in benzyl alcohol solution with acetonitrile as solvent under magnetic stirring condition in darkness for 12 h, and then separated by microfiltration and dried at 60 °C for 24 h. N<sub>2</sub> adsorption-desorption isotherms were analyzed on a nitrogen adsorption apparatus (Micromeritics ASAP 2020, USA).

### 2.3. Selective photocatalytic reaction

The selective photocatalytic activity of the as-prepared rutile TiO<sub>2</sub> samples was estimated by oxidation of benzyl alcohol into benzaldehyde in acetonitrile (Tianjin Guangfu Fine Chemical Research Institute). For each photocatalytic experiment, 10 mg of rutile TiO<sub>2</sub> samples were suspended in 2 ml of the 9.66 mmol l<sup>-1</sup> benzyl alcohol solution with acetonitrile as solvent under magnetic stirring condition. The photocatalytic reactions were carried out under the irradiation of xenon lamp (CEL-HXF 300, Techcomp) with a UV-cutoff filter ( $\geq 420 \text{ nm}$ ). In order to ensure sufficient interaction between the benzyl alcohol molecules and the rutile TiO<sub>2</sub> surface and facilitate adsorption of reactants and desorption of the products in the selective photocatalytic oxidation reaction, the solution was held under constant magnetic stirring condition during the whole photocatalytic process. After the photocatalytic reaction, the photocatalysts were separated out by centrifugation at 10,000 rpm rate. The quantitative identification of benzaldehyde concentration in solution was performed on Gas Chromatography (GC7890II, Techcomp) equipped with Flame Ionization Detector (FID). The photocatalysts were dried at 60 °C for 24 h and then were analyzed by FTIR to obtain information about the surface groups.

## 3. Results and discussion

### 3.1. Phase composition and crystallinity of samples

XRD patterns are recorded to identify the phase composition and crystallinity of the as-prepared samples as shown in Fig. 1.  $2\theta$  values of 27.45°, 36.09°, 39.19°, 41.23°, 44.05°, 54.34°, 56.64°, 62.74°, 69.01°, and 69.79° are corresponding to the diffractions of the (1 1 0), (1 0 1), (2 0 0), (1 1 1), (2 1 0), (2 1 1), (2 2 0), (0 0 2), (3 0 1), and (1 1 2) planes of rutile TiO<sub>2</sub> (tetragonal,  $P4_2/mnm$ , JCPDS No. 21-1276,  $a = b = 0.4593 \text{ nm}$  and  $c = 0.2959 \text{ nm}$ ). The main peaks of each sample are all very sharp, indicating good crystallinity and large crystallite size. No obvious difference is observed among the XRD patterns of the six samples, displaying the similar phase composition and crystallinity.

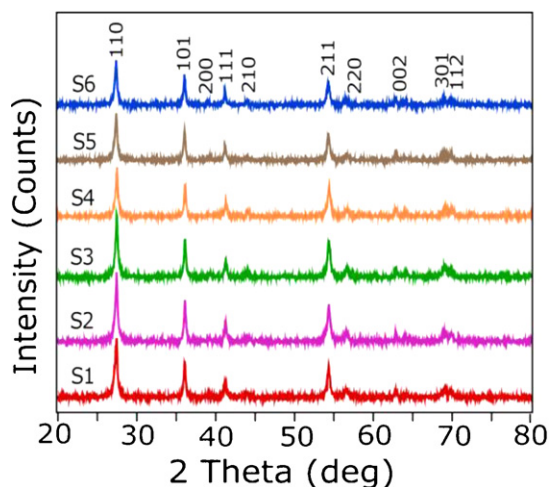


Fig. 1. XRD patterns for six samples.

### 3.2. Morphologies of rutile $\text{TiO}_2$ nanorods

The morphologies of the prepared rutile  $\text{TiO}_2$  samples were characterized by SEM first. The typical large-scale image shown in Fig. 2a displays the flower-like sample structure composed of nanorods with diameters of ca. 300 nm. For the nanorods of each sample, the distinctions among the fine morphologies can be observed from the high-resolution images of sample S1, S3, and S6 in Fig. 2b–d, which also reveal a successive growing process of the samples. For sample S1 (4-h growth time, Fig. 2b), the top part of the single nanorod is relatively flat. After 12-h reaction, the rutile  $\text{TiO}_2$  nanorod is divided into the shell and the core part (S3, Fig. 2c). The square shell is very compact with an about 80 nm-thickness smooth wall, while the middle part of the nanorod protrudes from the surface of the top to form the core. When the growth time reaches 24 h (S6), as shown in Fig. 2d, the top part of the single nanorod,

including both the core and the shell, split into a bundle of irregular rods with smaller diameters. The intermediate high-resolution image for S2, S4, and S5 with growth time at 8-, 16-, and 20-h, respectively, are shown in Fig. S2 in Supporting Information. It can be seen that no obvious difference in morphology can be observed after the growth time is longer than 16 h.

TEM images give more detailed information about the single nanorod. The low-resolution TEM images of S1, S3, and S6 are shown in Fig. S3 of Supporting Information. For sample S1, the top part looks smooth. And obvious shell and core on the top part are observed for sample S3. As for sample S6, the whole top part, including the shell and the core, split into more nanorods with smaller diameters. The above results are consistent with those obtained from SEM images. Zoomed-in TEM image for the core of sample S3 are shown in Fig. 2e, which indicates that the core is a bundle of single-crystalline rutile  $\text{TiO}_2$  nanorods with diameters of ca. 20 nm grow in  $[001]$  growth direction. More detailed examination of the nanorod with high-resolution TEM image in Fig. 2f demonstrates clear lattice fringes and the interplanar spacings of  $(110)$  and  $(001)$  planes are 3.25 Å and 2.95 Å, consistent with that for the rutile phase [34]. The inset shows the lattice fringes of the plane transformed by Fast Fourier Transform of Digital Micrograph software corresponding to the square area.

The formation of single-crystalline  $\text{TiO}_2$  nanorods can be attributed to the more active property of  $(001)$  plane, which results in the preferential growth of rutile  $\text{TiO}_2$  nanorods in  $[001]$  direction, and the addition of  $\text{Cl}^-$ , which could restrict the growth of  $(110)$  plane [35]. The split of the single nanorod shell of sample S5 and S6 is supposed to be derived from the different crystallite growth rates in  $(001)$  and  $(110)$  two main planes of the rutile  $\text{TiO}_2$ . Fig. S4 in Supporting Information exemplifies the crystallite sizes of the six samples in  $(001)$  and  $(110)$  planes at different growth time. With increasing growth time in the range of 4–24 h with the 4-h interval, the crystallite sizes of the six samples are calculated to be 19.9, 20.5, 21.6, 21.6, 23.7, and 25.5 nm in  $(001)$  plane, 37.3, 37.1, 36.8, 34.1, 41.4, and 64.3 nm in  $(110)$  plane, respectively, by

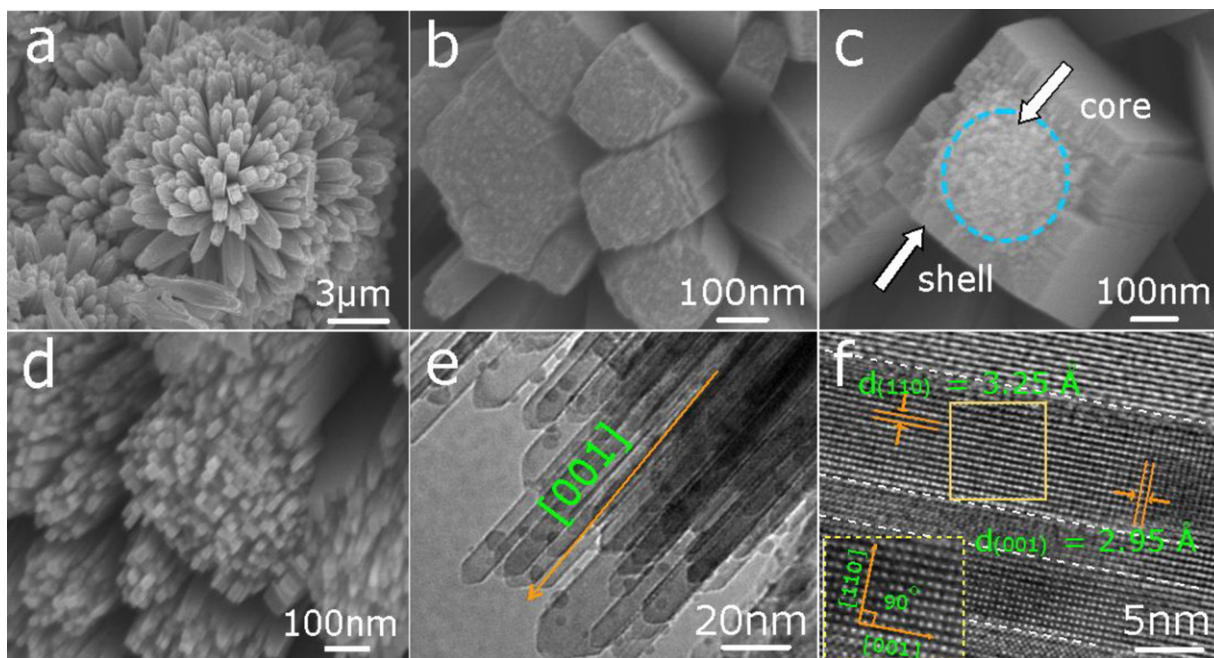
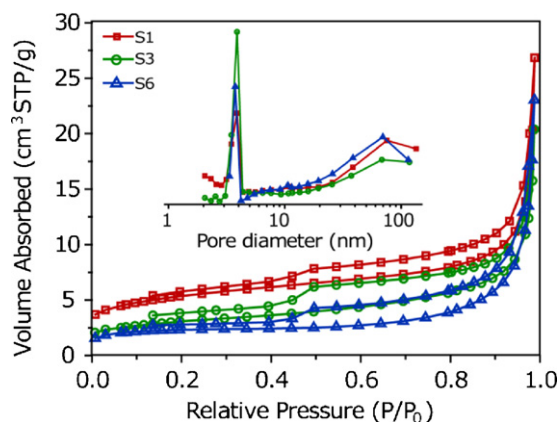


Fig. 2. The typical large-scale SEM image for samples (a), High-resolution SEM images of S1 (b), S3 (c), and S6 (d), Zoomed-in TEM images of the inner part of S3 (e), High-resolution TEM image of single nanorod (f). The inset shows the lattice fringes of the plane transformed by Fast Fourier Transform of Digital Micrograph software corresponding to the square area.





**Fig. 3.**  $N_2$  adsorption-desorption isotherms of sample S1, S3, and S6. The inset shows the corresponding pore size distribution curves.

the (1 1 0) and (0 0 2) facet diffraction peaks using the Scherrer formula [36]. It can be calculated that the crystallite size increases about 1–2 nm every 4 h in (0 0 1) plane, which is the same for sample S1–S4 in (1 1 0) plane. While for sample S5 and S6, the crystallite size increases 10–20 nm during the same interval time. So it is supposed that the faster growth of the crystallite in (1 1 0) plane results in the split of nanorods shell of sample S5 and S6.

### 3.3. $N_2$ adsorption-desorption analysis

$N_2$  adsorption-desorption isotherms and the corresponding pore size distribution curves of S1, S3, and S6 are shown in Fig. 3. For the representative three samples, the adsorption amount increases/decreases monotonously at a high  $P/P_0$  ( $P/P_0 > 0.9$ ) without an adsorption limitation. According to the International Union of Pure and Applied Chemistry (IUPAC) classification [37], the adsorption-desorption isotherms belong to type IV with hysteresis loops of H3. Type IV adsorption-desorption isotherms indicate the existence of mesopores (2–50 nm). Hysteresis loop of H3 is always correlated with slit-shaped pores [38]. Combined with SEM and TEM analysis, the formation of slit-like pores may be ascribed to both the formation of single-crystalline nanorods and the splitting process of the nanorod shell. In addition, at a relative high pressure range ( $P/P_0$  is ca. 1.0), the isotherms show very high absorption, suggesting the formation of large mesopores and macropores. Moreover, it can be found from the  $N_2$  adsorption isotherms that the adsorption amount of samples decrease from S1 to S6 at a low  $P/P_0$  ( $P/P_0 < 0.8$ ), indicating that the pore and crystallite size increase and the specific surface area decrease [39,40]. The pore size distribution curves of the three samples are shown in the inset of Fig. 3. It indicates that all the three samples expose mainly mesopores with a peak pore diameter of ca. 4 nm. However, the comparatively lower peaks at ca. 70 nm also suggest the existence of macropores.

**Table 1**

Samples	Hydrothermal reaction time (h)	$S_{\text{BET}}$ ( $\text{m}^2 \text{g}^{-1}$ )	Average pore size (nm)	Crystallite size <sup>a</sup> (nm)
S1	4	19.8	4.4	19.9
S2	8	15.8	7.0	20.5
S3	12	11.8	5.9	21.6
S4	16	11.1	6.1	21.6
S5	20	8.2	7.9	23.7
S6	24	8.9	8.1	25.5

<sup>a</sup> Crystallite sizes are determined by the broadening of the  $\text{TiO}_2$  (1 1 0) facet diffraction peak using the Scherrer formula.

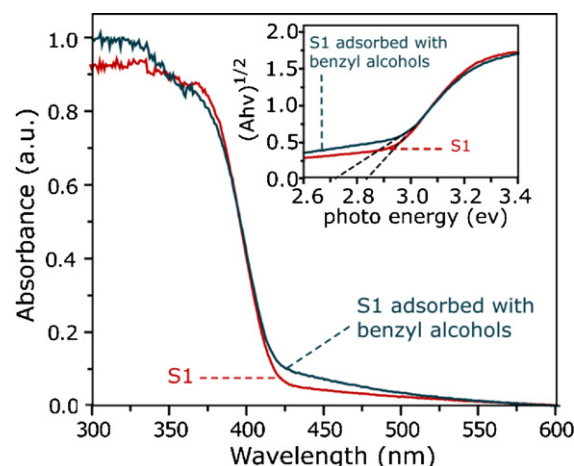


**Fig. 4.** UV-vis spectra of S1 and of S1 adsorbed with benzyl alcohols. The inset shows the plot of  $(Ah\nu)^{1/2}$  vs. photo energy.

The effect of hydrothermal reaction time on the physicochemical properties of the samples was summarized in Table 1. Roughly speaking, as the hydrothermal reaction time increases, the crystallite sizes of the samples increase, leading to the increased pore sizes. Moreover, the split of the single nanorod shell can further increase the pore sizes. The increased crystallite and pore sizes decrease the BET surface area.

### 3.4. Optical absorption properties

Visible-light-driven photocatalysts need to have optical absorption ability in the visible-light region. And since all samples are rutile  $\text{TiO}_2$  in our experiment, therefore, sample S1 is chosen as a representative sample to investigate the optical absorption properties. Fig. 4 shows the comparison of UV-vis absorption spectra of S1 and S1 adsorbed with benzyl alcohol. After adsorbed with benzyl alcohol, it is clearly revealed that the sample shows increased absorption intensity in 420–550 nm wavelength region and the corresponding absorption edge shifts (ca. 15 nm) toward a longer wavelength region. The absorption wavelength edge of semiconductors is determined by the bandgap energy ( $E_g$ ) [41]. Based on Kubelka-Munk function [42],  $E_g$  can be evaluated by the tangents to the plots of  $(Ah\nu)^{1/2}$  versus photo energy, where  $A$  is absorbance,  $h$  is Planck constant and  $\nu$  is the associated frequency, as shown in the inset in Fig. 4.  $E_g$  of sample S1 obtained from Fig. 4 is ca. 2.81 eV, smaller than 3.0 eV for rutile  $\text{TiO}_2$  [43], which can be ascribed to the impurities introduced during the preparation. After adsorbed with benzyl alcohol,  $E_g$  of the sample is reduced to ca. 2.71 eV. The bandgap narrowing can be assigned to the different excitation modes for the sample S1 and S1 adsorbed with benzyl alcohol. For the sample S1, the excitation mode is photo-induced direct excitation of  $\text{TiO}_2$  bandgap by the light in the UV region. For the sample S1 adsorbed with benzyl alcohol, a charge-transfer (CT) complex can form and be photo-excited by the light in the visible-light region corresponding to the narrowed bandgap due to the ligand-to-metal charge transfer (LMCT) [20,44,45]. In conclusion, the bandgap narrowing induces the redshift of the absorption edge and makes it possible to use visible light energy more effectively.

In our work, the higher visible-light absorption ability of the samples makes the selective photocatalytic oxidation of benzyl alcohol to be carried out under the visible-light irradiation. In addition, high surface-to-volume ratio and unique 1D channel of single-crystalline rutile  $\text{TiO}_2$  nanorods can help to disperse the electrons and furthermore facilitate the electron charge transfer

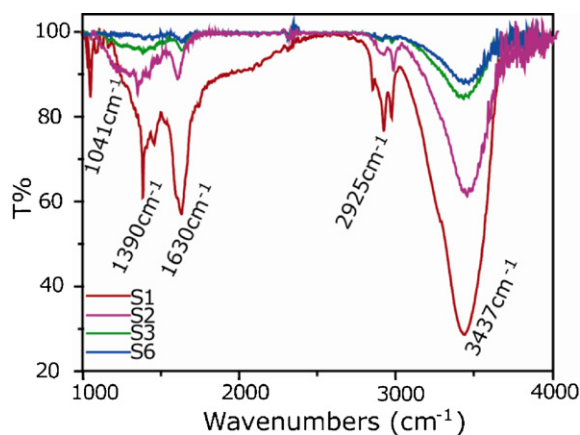


Fig. 5. FTIR spectra of sample S1, S2, S3, and S6.

from benzyl alcohol molecule to  $\text{TiO}_2$ , which favors the selective photocatalytic oxidation reaction.

### 3.5. FTIR spectra analysis

FTIR spectra of sample S1, S2, S3, and S6 are collected to obtain the related information about the surface properties (Fig. 5). Adsorption peaks at 1041 and 2925  $\text{cm}^{-1}$  correspond to C–O vibration and C–H stretching mode, respectively, which may be due to the residual titanium butoxide [46,47]. Actually, as hydrothermal reaction time increases, the intensity of these two peaks decreases sharply because the residual titanium butoxide decrease. The bands at 1390 and 1630  $\text{cm}^{-1}$  are ascribed to the adsorbed water, 3437  $\text{cm}^{-1}$  is assigned to the surface –OH group. Compared to the adsorption peak of the surface –OH group of anatase  $\text{TiO}_2$  (3657 and 3679  $\text{cm}^{-1}$ ) [25], there is a redshift of ca. 200  $\text{cm}^{-1}$  for the rutile  $\text{TiO}_2$  samples. The adsorption peaks of the surface –OH groups gradually decrease from sample S1 to S6, indicating that the surface –OH density decreases with the increase of hydrothermal reaction time during the preparation process. The surface –OH density can affect the selective photocatalytic activity, which will be examined by analysis of the results of the photocatalytic reaction in the following part.

### 3.6. Selective photocatalytic activity

The activity of the prepared single-crystalline rutile  $\text{TiO}_2$  nanorods on the conversion and selectivity for the oxidation of benzyl alcohols into benzaldehyde, are systematically investigated, as shown in Fig. 6. The graph of yields of benzaldehyde, which are calculated by the ratio of the concentration of benzaldehyde to the initial concentration of benzyl alcohol (9.66  $\text{mmol l}^{-1}$ ), at the different duration of visible light irradiation for the six samples is displayed in Fig. 6a, respectively. Obviously, the yields of benzaldehyde gradually increase with the extended irradiation time for each sample. At each fixed irradiation time, the yield of benzaldehyde first increases and then decreases, with sample S2 exhibiting the highest yield value. Combined with the FTIR analysis in Fig. 5, the selective photocatalytic activity first increases and then decreases for six samples (S1–S6), with S2 demonstrating the highest activity, as the surface hydroxyl group density increases. So, it can be concluded that there is an optimized value of the surface hydroxyl group density for the selective activity of the single-crystalline rutile  $\text{TiO}_2$  nanorods. Below the optimized value, the higher surface hydroxyl group density can enhance the hydrophilicity of  $\text{TiO}_2$  and promote desorption of the produced aldehyde, thus resulting in a high yield of aldehyde [19]. Above the optimized value, however,

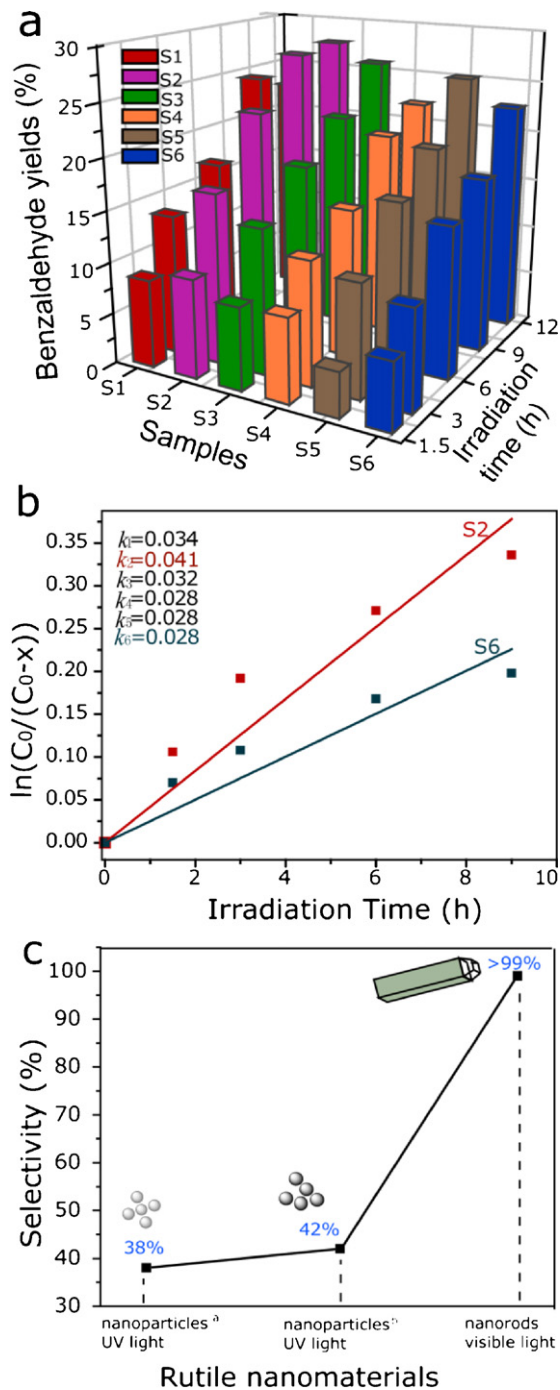


Fig. 6. (a) Graph of yields of benzaldehyde at the different duration of visible light irradiation for the six samples respectively, (b) the plot of  $\ln(C_0/(C_0-x))$  against irradiation time (h) ( $C_0$ : the initial concentration of benzyl alcohols,  $x$ : the concentration of benzaldehyde). (c) Comparison of selectivity for partial oxidation of benzyl alcohol over obtained rutile  $\text{TiO}_2$  nanorods under visible-light irradiation with the reported results for rutile nanoparticles under UV light irradiation.

it hinders the adsorption/desorption of both benzyl alcohol and benzaldehyde, rather than promote desorption of products, leading to a low yield of aldehyde. Summarily, the different morphologies of the rutile  $\text{TiO}_2$  nanorods leads to the different surface property and it is crucial for the selective photocatalytic activity. Therefore, control the hydrothermal reaction time to optimize the surface properties of the samples in the preparation of rutile  $\text{TiO}_2$  nanorods is an important factor in gaining higher selective photocatalytic activity.

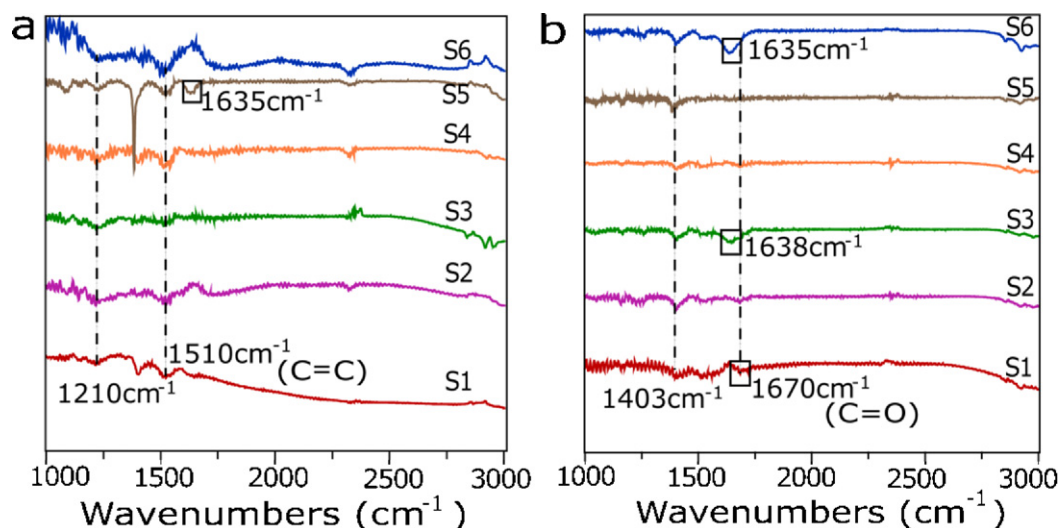


Fig. 7. FTIR spectra of the six samples after the photocatalytic reaction under visible-light irradiation for (a) 1.5 h and (b) 12 h.

Reaction kinetics of the selective photocatalytic oxidation of benzyl alcohol into benzaldehyde is studied for further understanding of the activities of the different samples. The photo-oxidation of benzyl alcohol is fitted into first-order reaction and the reaction rate constant ( $k$ ) can be evaluated from first-order reaction dynamics equation in Eq. (1):

$$\ln\left(\frac{C_0}{C_0 - x}\right) = kt \quad (1)$$

In the equation,  $C_0$  is the initial concentration of benzyl alcohol,  $x$  is the concentration of benzaldehyde and  $(C_0 - x)$  can be regarded as the concentration of benzyl alcohol due to the high selectivity of the reaction. The representative linear relationship between  $\ln(C_0/(C_0 - x))$  and  $t$  for sample S2 and S6 is shown in Fig. 6b, since these two samples correspond to the highest and the lowest  $k$  values, respectively. It is suggested that,  $k$  values first increase from 0.034 to 0.041 and then decrease from 0.041 to 0.028 for all samples, with S2 showing the highest value of 0.041, S4–S6 bear the same value of 0.028. Compared with Fig. 6a, it can be observed that the  $k$  values share the same changing trend with that of the selective photocatalytic activity.

During the oxidation reactions, only benzaldehyde is detected under the experimental conditions and the selectivity is over 99%. Thus, the selectivity of the prepared single-crystalline rutile  $\text{TiO}_2$  nanorods for the partial oxidation of benzyl alcohol under visible-light irradiation is much higher than that for rutile nanoparticles under UV light irradiation, which are only 38% [12] and 42% [19] as displayed in Fig. 6c.

In order to acquire information about the high selectivity, the representative FTIR spectra of the six samples after photocatalysis for 1.5 and 12 h are collected in Fig. 7, which are the shortest and longest irradiation time used in our experiment. The figure shows the adsorption intensity of benzyl alcohol and benzaldehyde of the samples during the reactions. In Fig. 7a,  $1210\text{ cm}^{-1}$  is attributed to the adsorbed water [25],  $1510\text{ cm}^{-1}$  is assigned to C=C stretching vibration of benzyl alcohol,  $1635\text{ cm}^{-1}$  of S5 is ascribed to the C=O stretching vibration of benzaldehyde, which is not apparent for other samples, however. In Fig. 7b, the peak at  $1403\text{ cm}^{-1}$  is ascribed to the adsorbed water,  $1635$ ,  $1638$  and  $1670\text{ cm}^{-1}$  are assigned to be the characteristic peaks of C=O stretching vibration of benzaldehyde. The difference of the wavenumbers of the same group may be caused by the different surface properties of samples. As a complement, FTIR spectra of six samples after the adsorption/desorption in benzyl alcohol/acetonitrile solution for

2 h in darkness is also obtained, which is shown in Fig. S5. Compared with that in Fig. 7, no obvious and consistent peaks for six samples are observed in Figure S5, which indicates that, the adsorption of benzyl alcohol on the samples is not strong. This can be explained as follows. The binding ability between benzyl alcohol molecule and the surface of samples is not very strong, and adsorption reaches the saturation point by only a small amount of benzyl alcohol. Under the visible light irradiation, the adsorbed benzyl alcohol is oxidized into benzaldehyde, which makes further adsorption. It can be observed from the FTIR spectra that, compared with that on  $\text{TiO}_2$  nanoparticles [21], the adsorption of benzyl alcohol and benzaldehyde are not very strong on the obtained single-crystalline rutile  $\text{TiO}_2$  nanorods surfaces which are mainly composed of (1 1 0) plane. Therefore, it is supposed that, compared with nanoparticles, the high surface-to-volume ratio of  $\text{TiO}_2$  nanorods supplies more sites for the interaction of organic molecules with the surface of samples and facilitates the adsorption and desorption of benzyl alcohol and benzaldehyde molecules, thus results in a high selective photocatalytic oxidation of benzyl alcohol.

### 3.7. Mechanism

A tentative mechanism of selective photocatalytic oxidation of benzyl alcohol to benzaldehyde over single-crystalline rutile  $\text{TiO}_2$  nanorods was proposed as illustrated in Fig. 8. The main surface of rutile  $\text{TiO}_2$  is (1 1 0) plane, which has the thermodynamically most stable structure, more ideal for study of the organic adsorption mode due to the stability [48,49]. The surface atom distribution consists of  $\text{Ti}_{5c}$  (fivefold coordinated) and  $\text{O}_{2c}$  (twofold coordinated) atoms [50]. The loss of oxygen atoms from  $\text{O}_{2c}$  rows can lead to the formation of oxygen vacancies, which plays a very important role in the surface properties on  $\text{TiO}_2$  (1 1 0) surface. The dissociation of water on  $\text{O}_{2c}$  atom rows will lead to the formation of some hydroxyl groups on the surface, which are closely related to selective photocatalytic oxidation of organic molecules [51]. In our study, it is proposed that benzyl alcohol molecules are attracted to the surface of rutile  $\text{TiO}_2$  (1 1 0) firstly which may be attributed to the interaction between the –OH group of benzyl alcohol and –OH group of  $\text{O}_{2c}$  atoms row. Then the H of –OH is dissociated and combined with  $\text{O}_{2c}$  atom to form hydroxyl groups and the O of –OH group interacts with  $\text{Ti}_{5c}$  to form a surface complex with an electron transfer to  $\text{Ti}_{5c}$ , which is consistent with the adsorption mode of many organic molecules containing –OH groups, such as oxalic acid/oxalate [52,53], methyl phosphonic acid [54], Catechol [49],



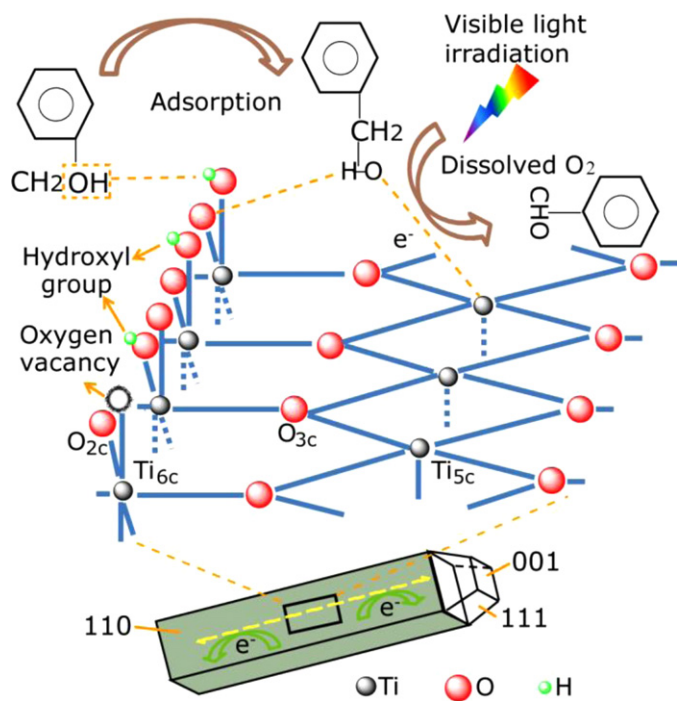


**Fig. 8.** A tentative schematic illustration for the reaction of selective photocatalytic oxidation of benzyl alcohol into benzaldehyde over rutile  $\text{TiO}_2$  nanorods under visible-light irradiation.

and ethanol molecule [55] on rutile  $\text{TiO}_2$  (1 1 0) surface. The surface complex can generate holes ( $h^+$ ) and electrons ( $e^-$ ) under visible-light irradiation [20]. The electrons are captured by the dissolved oxygen. Due to the attraction of holes,  $\text{PhCH}_2\text{O}$  (being adsorbed) releases another H atom and electron to form benzaldehyde. Moreover, rutile  $\text{TiO}_2$  nanorods demonstrate many advantages for the selective photocatalytic oxidation of benzyl alcohol compared with nanoparticles. Firstly, the high surface-to-volume ratio allows for the interaction of benzyl alcohol molecules with the surface of samples more readily. Secondly, due to the unique property of unidirectional channel for electron charge transport on (1 1 0) plane of single-crystalline rutile  $\text{TiO}_2$  nanorods, the electrons transferred to  $\text{Ti}_{5c}$  can be dispersed more efficiently, facilitating the electron charge transport from the benzyl alcohol molecules to  $\text{TiO}_2$  nanorods. Additionally, rutile  $\text{TiO}_2$  nanorods exhibit superior survivability of electrons and extend the corresponding lifetime, thus can suppress the photogenerated electrons to combine with the trapped holes [31]. All these characteristics favor the selective photocatalytic oxidation extraordinarily.

#### 4. Conclusions

In summary, selective photocatalytic oxidation of benzyl alcohol into benzaldehyde under visible-light irradiation over single-crystalline rutile  $\text{TiO}_2$  nanorods was systematically studied. The nanorods were prepared by a hydrothermal reaction using rutile  $\text{TiO}_2$  as a substrate at  $150^\circ\text{C}$ . In the presence of the obtained rutile  $\text{TiO}_2$  nanorods, benzyl alcohol is oxidized into benzaldehyde with a very high selectivity. Generally speaking, as hydrothermal reaction time increases, the crystallite size increases, the BET surface area and the surface hydroxyl group density decrease gradually and the selective photocatalytic activity increases first and then decreases with sample S2 shows the highest value. A tentative mechanism is proposed that the visible-light-driven selective photocatalytic activities are due to visible-light absorption ability of benzyl alcohol- $\text{TiO}_2$  complex and the unique properties of rutile

$\text{TiO}_2$  nanorods, such as high surface-to-volume ratio, unidirectional 1D channel and superior survivability of electrons, may contribute to the more efficient electrons transport, which is further helpful for the formation of benzaldehyde. Our research opens up a new perspective for the selective photocatalytic oxidation of aromatic alcohols over one-dimensional rutile  $\text{TiO}_2$  nanomaterials instead of limiting to commonly used nanoparticles, having great potential for green synthesis and high-efficiency energy conversion.

#### Acknowledgments

This work was supported by the National Basic Research Program of China (Nos. 2011CB933401 and 2012CB934000) and the National Natural Science Foundation of China (Nos. 21005023 and 91123003). J.R. Gong also gratefully acknowledges the support of Special Presidential Foundation of Chinese Academy of Sciences and K. C. Wong Education Foundation, Hong Kong.

#### Appendix A. Supplementary data

Supplementary data associated with this article can be found, in the online version, at doi:10.1016/j.apcatb.2011.12.003.

#### References

- [1] R. Asahi, T. Morikawa, T. Ohwaki, K. Aoki, Y. Taga, *Science* 293 (2001) 269.
- [2] G. Kuzmanich, A. Natarajan, K.K. Chin, M. Veerman, C.J. Mortko, M.A. Garcia-Garibay, *J. Am. Chem. Soc.* 130 (2008) 1140–1141.
- [3] B. O'regan, M. Gr-tzel, *Nature* 353 (1991) 737–740.
- [4] N.C. Jeong, O.K. Farha, J.T. Hupp, *Langmuir* 27 (2011) 1996–1999.
- [5] C.Y. Lee, C. She, N.C. Jeong, J.T. Hupp, *Chem. Commun.* 46 (2010) 6090–6092.
- [6] N. Alenzi, W.S. Liao, P.S. Cremer, V. Sanchez-Torres, T.K. Wood, C. Ehlig-Economides, Z. Cheng, *Int. J. Hydrogen Energy* 35 (2010) 11768–11775.
- [7] C. Falkenberg, S. Olthof, R. Rieger, M. Baumgarten, K. Muellen, K. Leo, M. Riede, *Sol. Energy Mater. Sol. Cells* 95 (2011) 927–932.
- [8] Q. Li, B. Guo, J. Yu, J. Ran, B. Zhang, H.J. Yan, J.R. Gong, *J. Am. Chem. Soc.* 133 (2011) 10878–10884.
- [9] G. Palmisano, M. Addamo, V. Augugliaro, T. Caronna, E. García-López, V. Loddo, L. Palmisano, *Chem. Commun.* (2006) 1012–1014.
- [10] G. Palmisano, S. Yurdakal, V. Augugliaro, V. Loddo, L. Palmisano, *Adv. Synth. Catal.* 349 (2007) 964–970.
- [11] V. Augugliaro, H. Kisch, V. Loddo, M.J. López-Muñoz, C. Márquez-Álvarez, G. Palmisano, L. Palmisano, F. Parrino, S. Yurdakal, *Appl. Catal. A* 349 (2008) 182–188.
- [12] S. Yurdakal, G. Palmisano, V. Loddo, V. Augugliaro, L. Palmisano, *J. Am. Chem. Soc.* 130 (2008) 1568–1569.
- [13] D.I. Enache, J.K. Edwards, P. Landon, B. Solsona-Espriu, A.F. Carley, A.A. Herzog, M. Watanabe, C.J. Kiely, D.W. Knight, G.J. Hutchings, *Science* 311 (2006) 362–365.
- [14] S. Li, U. Diebold, *J. Am. Chem. Soc.* 132 (2010) 64–66.
- [15] G. Palmisano, E. García-López, G. Marci, V. Loddo, S. Yurdakal, V. Augugliaro, L. Palmisano, *Chem. Commun.* 46 (2010) 7074–7089.
- [16] Y. Jang, S. Kim, S.W. Jun, B.H. Kim, S. Hwang, I.K. Song, B.M. Kim, T. Hyeon, *Chem. Commun.* 47 (2011) 3601–3603.
- [17] M. Zhang, Q. Wang, C. Chen, L. Zang, W. Ma, J. Zhao, *Angew. Chem. Int. Ed.* 48 (2009) 6081–6084.
- [18] Q. Wang, M. Zhang, C. Chen, W. Ma, J. Zhao, *Angew. Chem. Int. Ed.* 49 (2010) 7976–7979.
- [19] S. Yurdakal, G. Palmisano, V. Loddo, O. Alagoz, V. Augugliaro, L. Palmisano, *Green Chem.* 11 (2009) 510–516.
- [20] S. Higashimoto, N. Kitao, N. Yoshida, T. Sakura, M. Azuma, H. Ohue, Y. Sakata, *J. Catal.* 266 (2009) 279–285.
- [21] V. Augugliaro, V. Loddo, M.J. López-Muñoz, C. Márquez-Álvarez, G. Palmisano, L. Palmisano, S. Yurdakal, *Photochem. Photobiol. Sci.* 8 (2009) 663–669.
- [22] V. Augugliaro, T. Caronna, V. Loddo, G. Marci, G. Palmisano, L. Palmisano, S. Yurdakal, *Chem. Eur. J.* 14 (2008) 4640–4646.
- [23] V. Augugliaro, L. Palmisano, *ChemSusChem* 3 (2010) 1135–1138.
- [24] J.T. Carneiro, C.C. Yang, J.A. Moulijn, G. Mul, *J. Catal.* 277 (2011) 129–133.
- [25] J.T. Carneiro, A.R. Almeida, J.A. Moulijn, G. Mul, *Phys. Chem. Chem. Phys.* 12 (2010) 2744–2750.
- [26] M.D. Hernández-Alonso, A.R. Almeida, J.A. Moulijn, G. Mul, *Catal. Today* 143 (2009) 326–333.
- [27] M. Zhang, C. Chen, W. Ma, J. Zhao, *Angew. Chem. Int. Ed.* 47 (2008) 9730–9733.
- [28] S. Higashimoto, N. Suetsugu, M. Azuma, H. Ohue, Y. Sakata, *J. Catal.* 274 (2010) 76–83.
- [29] S. Higashimoto, K. Okada, T. Morisugi, M. Azuma, H. Ohue, T.H. Kim, M. Matsumoto, M. Anpo, *Top. Catal.* 53 (2010) 578–583.
- [30] Q. Zeng, L. Wu, Y. Zhang, B. Qi, J. Zhi, *Scr. Mater.* 62 (2010) 810–813.

- [31] J.H. Bang, P.V. Kamat, *Adv. Funct. Mater.* 20 (2010) 1970–1976.
- [32] Y. Liu, H. Wang, Y. Wang, H. Xu, M. Li, H. Shen, *Chem. Commun.* 47 (2011) 3790–3792.
- [33] E. Bae, T. Ohno, *Appl. Catal. B* 91 (2009) 634–639.
- [34] E. Bae, N. Murakami, M. Nakamura, T. Ohno, *Appl. Catal. A* 380 (2010) 48–54.
- [35] B. Liu, E.S. Aydil, *J. Am. Chem. Soc.* 131 (2009) 3985–3990.
- [36] A. Patterson, *Phys. Rev.* 56 (1939) 978–982.
- [37] K. Sing, D. Everett, R. Haul, L. Moscou, R. Pierotti, J. Rouquerol, T. Siemieniowska, *Pure Appl. Chem.* 57 (1985) 603–619.
- [38] J. Yu, Q. Xiang, J. Ran, S. Mann, *CrystEngComm* (2009) 872–879.
- [39] K. Lv, J. Yu, K. Deng, J. Sun, Y. Zhao, D. Du, M. Li, *J. Hazard. Mater.* 173 (2010) 539–543.
- [40] J. Yu, J. Fan, L. Zhao, *Electrochim. Acta* 55 (2010) 597–602.
- [41] H. Yu, H. Irie, K. Hashimoto, *J. Am. Chem. Soc.* 132 (2010) 6898–6899.
- [42] F. Dong, S. Guo, H. Wang, X. Li, Z. Wu, *J. Phys. Chem. C* 115 (2011) 13285–13292.
- [43] U. Diebold, S.C. Li, M. Schmid, *Annu. Rev. Phys. Chem.* 61 (2010) 129–148.
- [44] T. Tachikawa, S. Tojo, M. Fujitsuka, T. Majima, *Langmuir* 20 (2004) 2753–2759.
- [45] Y. Wang, K. Hang, N.A. Anderson, T. Lian, *J. Phys. Chem. B* 107 (2003) 9434–9440.
- [46] T. Jiang, Q. Zhao, M. Li, H. Yin, *J. Hazard. Mater.* 159 (2008) 204–209.
- [47] Y. Li, X. Sun, H. Li, S. Wang, Y. Wei, *Powder Technol.* 194 (2009) 149–152.
- [48] N. Shibata, A. Goto, S.Y. Choi, T. Mizoguchi, S. Findlay, T. Yamamoto, Y. Ikuhara, *Science* 322 (2008) 570–573.
- [49] S.C. Li, L.N. Chu, X.Q. Gong, U. Diebold, *Science* 328 (2010) 882–884.
- [50] Z. Dohnálek, I. Lyubinetsky, R. Rousseau, *Prog. Surf. Sci.* 85 (2010) 161–205.
- [51] Z. Zhang, R. Rousseau, J. Gong, S.C. Li, B.D. Kay, Q. Ge, Z. Dohnálek, *Phys. Rev. Lett.* 101 (2008) 156103.
- [52] C.B. Mendive, T. Bredow, A. Feldhoff, M. Blesa, D. Bahnemann, *Phys. Chem. Chem. Phys.* 10 (2008) 1960–1974.
- [53] C.B. Mendive, T. Bredow, A. Feldhoff, M.A. Blesa, D. Bahnemann, *Phys. Chem. Chem. Phys.* 11 (2009) 1794–1808.
- [54] C. Pang, M. Watkins, G. Cabailh, S. Ferrero, L. Ngo, Q. Chen, D. Humphrey, A. Schluger, G. Thornton, *J. Phys. Chem. C* 114 (2010), 16983–16980.
- [55] A. Nadeem, J. Muir, K. Connelly, B. Adamson, B. Metson, H. Idriss, *Phys. Chem. Chem. Phys.* 13 (2011) 7637–7643.